The Hotel Payload 2 campaign: Overview of NO, O and electron density measurements in the upper mesosphere and lower thermosphere

Carl-Fredrik Enell[a,*], Jonas Hedin[b], Jacek Stegman[b], Georg Witt[b], Martin Friedrich[c], Werner Singer[d], Gerd Baumgarten[d], Bernd Kaifler[d], Ulf-Peter Hoppe[e], Björn Gustavsson[f], Urban Brändström[g], Mikhail Khaplanov[b], Antti Kero[a], Thomas Ulich[a], Esa Turunen[h]

[a]*Sodankylä Geophysical Observatory, University of Oulu, Sodankylä, Finland*
[b]*Department of Meteorology, Stockholm University, Sweden*
[c]*Graz University of Technology, Austria*
[d]*Leibniz-Institute of Atmospheric Physics, Rostock University, Kühlungsborn, Germany*
[e]*Norwegian Defence Research Establishment, Kjeller, Norway*
[f]*University of Southampton, UK*
[g]*Swedish Institute of Space Physics, Kiruna, Sweden*
[h]*European Incoherent Scatter Scientific Association, Kiruna, Sweden*

Abstract

The ALOMAR eARI Hotel Payload 2 (HotPay 2) rocket campaign took place at Andøya Rocket Range, Norway, in January 2008. The rocket was launched on January 31, 2008 at 19:14 UT, when auroral activity appeared after a long geomagnetically quiet period. In this paper we present an overview of the HotPay2 measurements of upper mesospheric and lower thermospheric (UMLT) electron, atomic oxygen (O) and nitric oxide (NO) densities. [O] and [NO] were retrieved from a set of three photometers, Night-Time Emissions from the Mesosphere and Ionosphere (NEMI). Faraday rotation receivers on the rocket and the EISCAT UHF incoherent scatter radar provided simultaneous electron density profiles whereas the ALOMAR Na lidar and meteor radar measured the temperature profile and wind. The aurora was also observed with ground-based imagers.

*Corresponding author. Address: Sodankylä Geophysical Observatory, Tähteläntie 62, FIN-99600 Sodankylä, Finland

Email addresses: carl-fredrik.enell@sgo.fi (Carl-Fredrik Enell), jonash@misu.su.se (Jonas Hedin)

Preprint submitted to J. Atmospheric and Solar-Terrestrial Physics *January 11, 2011*

The retrieved oxygen number density profile has a maximum at 89 kilometres, some 10 km lower than expected from earlier measurements and modelled profiles based on climatological averages (such as the MSIS model), and the retrieved NO densities are also lower than expected. Satellite measurements indicate that subsidence over the winter pole controlled the densities. Quantitative chemistry model results based on climatological average atmospheric density and temperature profiles were therefore not in good agreement with the measured profiles. The Hotel Payload 2 measurements thus confirm the importance of downward transport from the thermosphere into the winter polar vortex.

Keywords: nitric oxide, oxygen, ionosphere, UMLT

---

1. Introduction

1.1. Chemistry of the UMLT region

The upper mesosphere and lower thermosphere (UMLT), at some 80–150 km above the ground, is a region where the weakly ionised plasma of the ionospheric D and E layers and the neutral components of the middle atmosphere interact. In the auroral zone, ionisation and dissociation of species in the UMLT is not only by photochemistry but also by low- to medium-energetic electron and proton precipitation. In this way the composition of the polar atmosphere depends on auroral activity, as discussed below.

Atomic oxygen is the major carrier of chemical energy in the mesosphere and lower thermosphere. It is produced in the upper atmosphere through O_2 photolysis during the day and recombines during the night to form molecular oxygen in a number of metastable states. These excited states will then emit radiation or be quenched to lower lying states by e.g. O_2, N_2 or O, giving rise to nightglow emissions covering the spectral range from the UV to the IR (e.g. Meriwether Jr., 1989).

Nitric oxide (NO) is another species of major importance in the middle and upper atmosphere. In the lowermost ionosphere NO^+ is the main ionised species, produced both by direct photoionisation and from the short-lived main primary ions O_2^+, O^+ and N_2^+ by charge exchange reactions. Downward transport of NO from the UMLT has also been shown to be important. Further down in the middle atmosphere conversion between NO and NO_2 takes place, total NO_x=(N+NO+NO_2) being long-lived in the winter polar vortex where it e.g. destroys ozone, which in turn changes the temperature

profile. Several studies (see Seppälä et al., 2007; Seppälä, 2007) suggest that this effect of the subsidence of NO_x affects the stability of the atmosphere down to the stratosphere. This may at least in part be the reason why ground temperatures correlate with auroral activity (Seppälä et al., 2009).

The Hotel Payload 2 rocket, as described in the following section, carried instruments for measuring the atomic oxygen, nitric oxide and electron density profiles, and simultaneously campaign measurements with ground-based incoherent scatter radar (ISR) and optical instruments were undertaken. In this paper an overview of these measurements is given and the results are compared with models and satellite measurements.

1.2. The ALOMAR eARI Hotel Payload launches

With EU FP6 funding, Andøya Rocket Range in northern Norway (69.3° N, 16.0° E) launched two so-called hotel payload (HotPay) rockets, HotPay 1 and HotPay 2. HotPay 2 was a two-stage rocket to be launched during the winter season (polar night). Due to the nature of the hotel payload concept the project became a tradeoff between research groups with diverse scientific objectives. The rocket carried in total nine different instruments, out of which some were aimed for studying the upper mesosphere and lower thermosphere (UMLT) region whereas others required a high apogee. The latter were a cosmic ray spectrometer from the Bulgarian Academy of Sciences, an electron detector from the Slovak academy of sciences, and two French instruments aimed for studying waves, a search coil magnetometer from Centre d'étude des Environnements Terrestre et Planétaires (CETP) and a current loop from Laboratoire de Physique et Chimie de l'Environnement et de l'Espace (LPC2E). This paper, however, concentrates on the results from the UMLT instruments, which are described in detail below. A collaborative Finnish-Swedish-UK European Incoherent Scatter (EISCAT) radar and optical ground-based measurement campaign was organised during the rocket campaign with several objectives: observing the aurora and ionosphere before and after the launch, modulating the ionospheric D region with the EISCAT Heating facility (Rietveld et al., 1992), and comparisons of high-altitude winds derived from the tristatic EISCAT UHF radar and Fabry-Perot interferometers measuring the Doppler shift of the $O(^1S)$ emission at 630 nm.

During the pre-launch meetings and discussions a compromise was agreed upon: to launch the rocket after auroral activity and preferably over a stable auroral arc, providing a dark background on the upleg and if possible flying through the aurora on the downleg. The HotPay 2 campaign took place

in January–February 2008. After a long geomagnetically quiet period the desired conditions were met on 2008-01-31, with clear skies over northern Scandinavia and auroral activity with a stable arc moving south over Andøya around 18 UT (see the magnetograms in Fig. 1). The HotPay 2 rocket was launched at 19:14 UT. During the flight the aurora was weak north of Andøya, activating only after 21 UT (not shown in the figure). The rocket trajectory was calculated from the on-board magnetometers and the WMM 2005 magnetic field model (McLean et al., 2004). Fig. 2 shows a 2-dimensional map projection of the trajectory. The rocket reached an apogee of 377 km over the North Atlantic. In the upleg the upper mesosphere and lower thermosphere (UMLT) region, 75–150 km above the ground, was traversed at a latitude of around 69.5 degrees, i.e. close to the launch site and also close to the latitude of the EISCAT radar site at Ramfjordmoen near Tromsø, where the ground-based radar measurements took place. During descent the rocket started falling over already at an altitude of some 150 km, rendering the downleg data unsuitable for further analysis.

The HotPay2 instruments of relevance to the UMLT region were Faraday rotation receivers and a positive-ion probe for measuring electron and ion density profiles (Mechtly et al., 1967; Jacobsen and Friedrich, 1979), a charged mesospheric dust particle detector(Lynch et al., 2005), two photometers for the sodium doublet at 589.0 and 589.6 nm, which unfortunately failed during the launch, and the main UMLT instrument, a set of three photometers named NEMI, Night-Time emissions from the Mesosphere and Ionosphere, built at the Department of Meteorology of Stockholm University (MISU) in collaboration with Sodankylä Geophysical Observatory, University of Oulu, Finland (SGO).

2. The NEMI photometers

The three NEMI photometers were standard filter photometers (Fig. 3) optimised for the detection of

- The oxygen atmospheric band emission at 762 nm, for retrieving the atomic oxygen density profile
- The N_2^+ first negative band emission in the (0-0) line at 391.4 nm, which is a direct measure of auroral electron precipitation
- The NO_2 continuum emission at 540 nm, for retrieval of the NO density profile

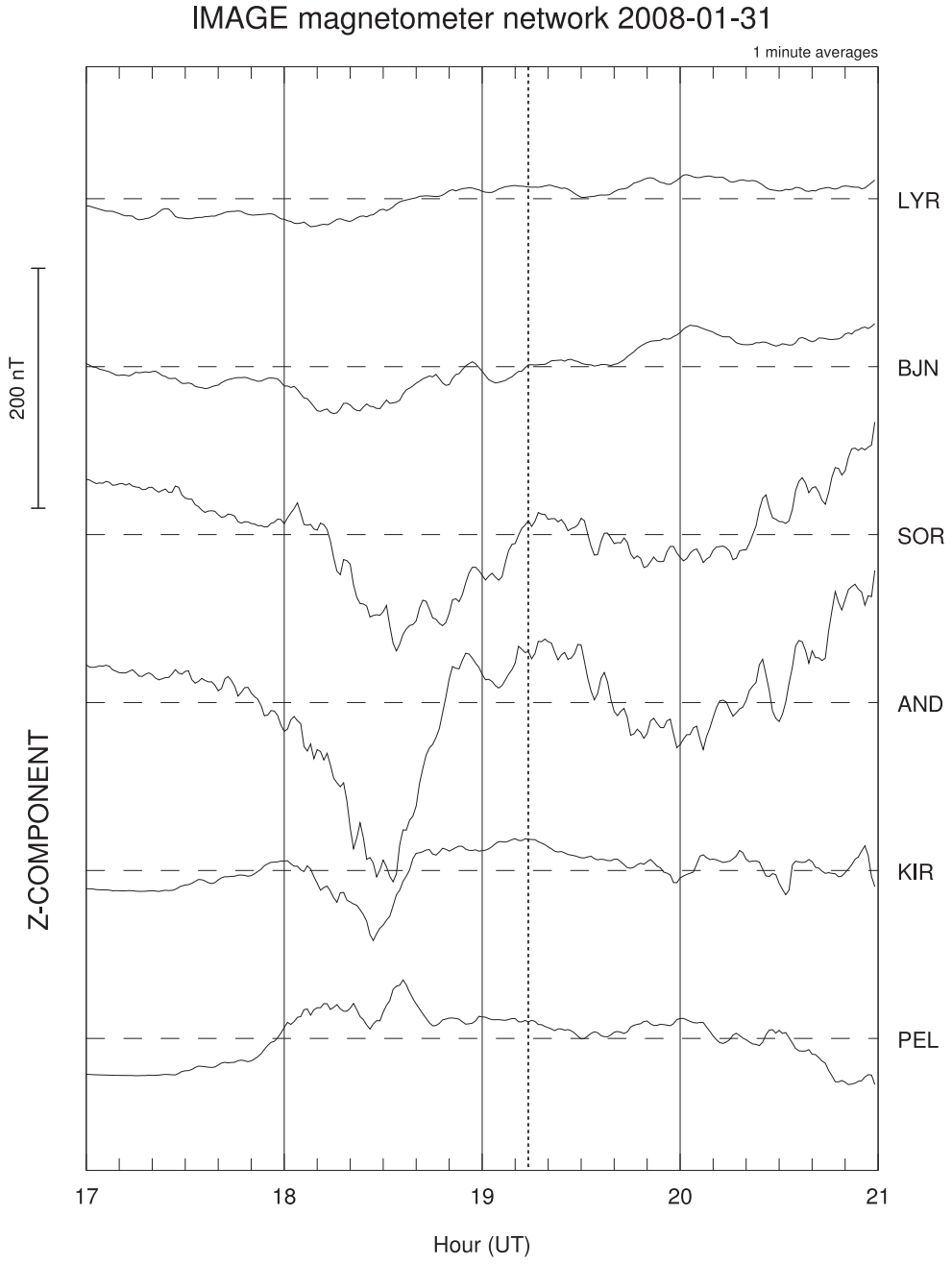

Figure 1: Magnetograms from the IMAGE magnetometer network stations at Longyearbyen, Bjørnøya (Bear Island), Sørøya, Andenes and Kiruna, showing the vertical component (Z). Weak auroral activity with a stable arc moving south started before 18 UT and the rocket was subsequently launched at 19:14 UT (dotted vertical line). During the flight the activity was weak. Not shown in this scale is the activation and breakup that occurred after 21 UT.

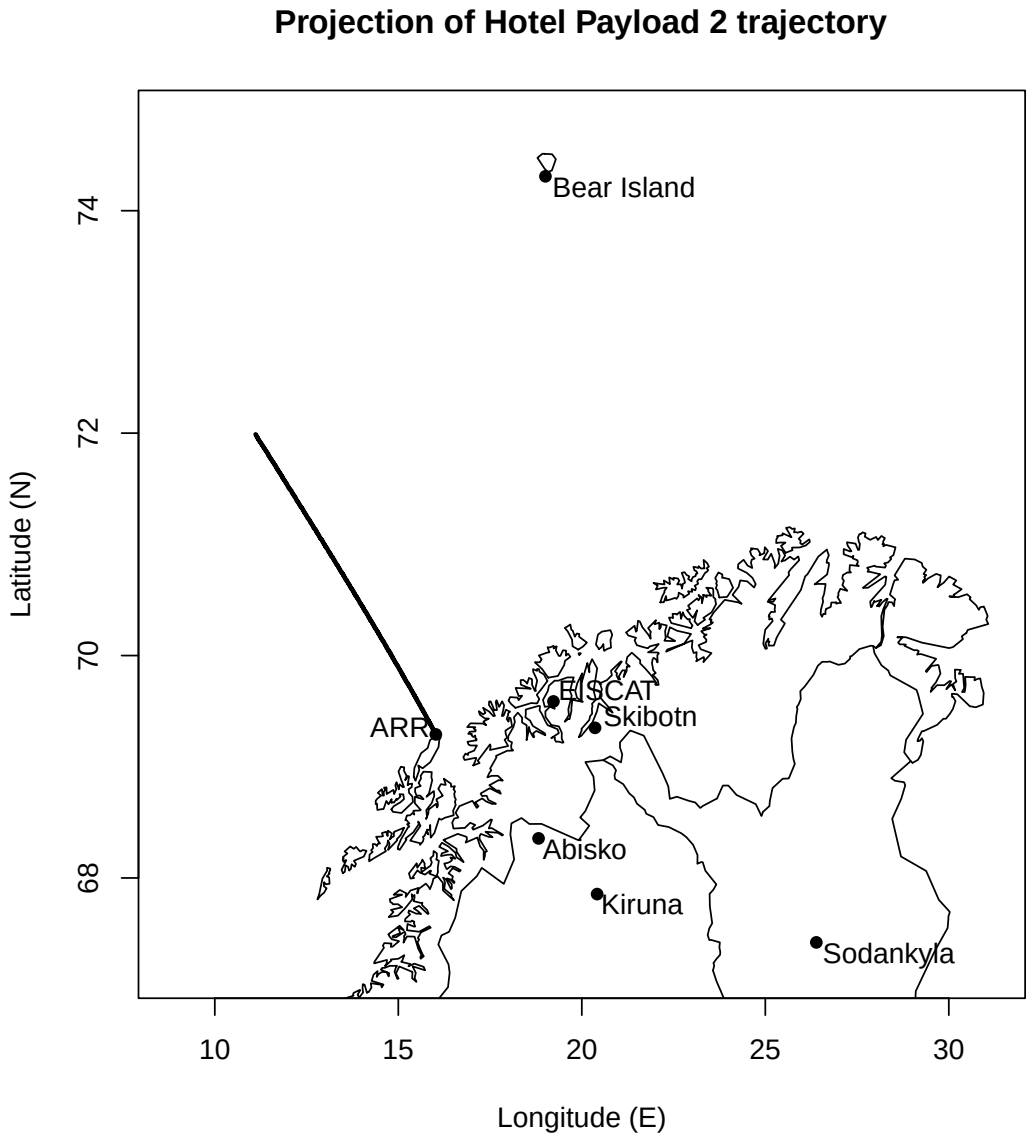

Figure 2: The Hotel Payload 2 trajectory from Andøya Rocket Range (ARR): 2-D projection on a map of northern Scandinavia. Also marked are the locations of the EISCAT transmitter and receiver sites, the ALIS auroral imager stations at Abisko and Skibotn mentioned in the text, and Bjørnøya (Bear Island) to show the latitude scale of the flight. The UMLT region was traversed at approximately the same latitude as that of the EISCAT transmitter station.

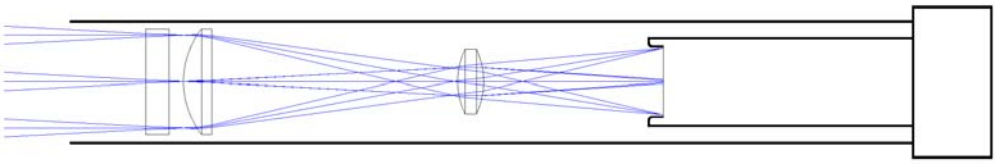

Figure 3: The design of the NEMI photometers. From left to right the interference filter, telescope lenses and photomultiplier tube are seen. Also shown is a ray tracing over the field of view.

On the rocket payload the photometers were positioned under the nose cone, looking in the forward direction along the rocket axis. Each photometer had its own pulse amplifier and counter, connected to the rocket telemetry system. For the conversion of count rates to radiances both the spectral response and the absolute sensitivity of the three photometers were calibrated in the MISU laboratory before launch.

3. NEMI analysis and results

After the flight the NEMI count rate profiles were corrected for the so-called van Rhijn effect (van Rhijn, 1921), i.e. converted to corresponding zenith rates as function of rocket attitude angle under the assumption that the emissions are horizontally homogeneous. This can be assumed to be valid for small coning angles of the rocket. In the absence of auroral emissions in the field of view, there is still a weak inhomogeneous background from stars and zodiacal light. This background was removed and the profiles were then converted from counts to absolute radiance using the pre-flight laboratory calibrations. Fig. 4 shows the radiance profiles thus obtained for the three photometers, in 1-km averages with 1-sigma error bars. To check the validity of the calibration, the 1N total zenith radiance which corresponds to some 500 Rayleighs was also checked against simultaneous 427.8 nm data from the Auroral Large Imaging System (ALIS) stations (Brändström, 2003) with fields of view closest to Andøya, Skibotn, Norway and Abisko, Sweden (marked on the map in Fig.2). During the flight no evident auroral emissions were observed and thus the data are not shown here. This means that the 1N radiance was well below the uncertainties in ALIS CCD bias and dark count rates, or significantly lower than 500 R. The 391.4 nm radiance measured by NEMI is therefore likely within the expected ratio (≈ 3) to the 427.8 nm radiance (Vallance-Jones, 1974).

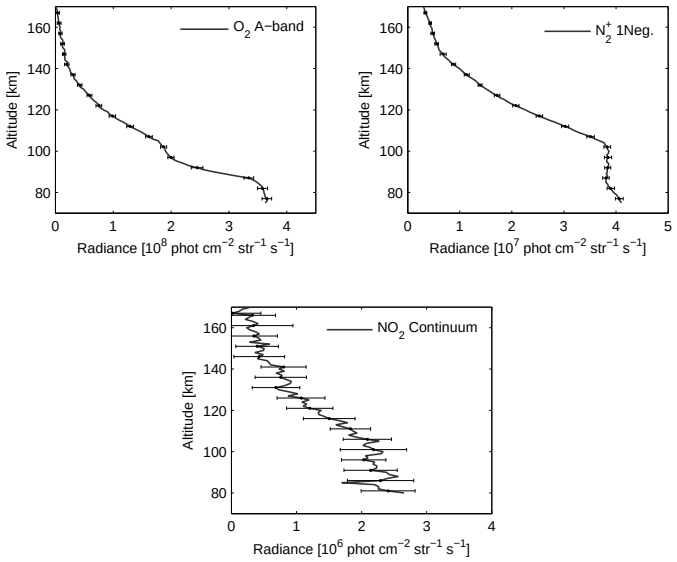

Figure 4: NEMI equivalent zenith radiance profiles, 1-km averages, corrected for dark counts and extra-atmospheric background light. Error bars show 1 standard deviation.

The radiance profiles were smoothed and numerically differentiated to yield volume emission rate profiles. The volume emission rates from the three NEMI photometers are shown in Fig. 5. In the following the retrieval of oxygen and nitric oxide profiles is described.

3.1. O profile retrieval

The atmospheric band system of O_2 $\left(b^1\Sigma_g^+ \rightarrow X^3\Sigma_g^-\right)$ is one of the strongest emission features in the night sky spectrum and is dominated by the (0-0) and (0-1) bands at 762 nm and 864 nm, respectively. To derive the atomic oxygen concentration from this emission, results from the ETON (Energy Transfer in the Oxygen Nightglow) rocket campaign in 1982 (Greer et al., 1986) were used. The ETON rocket campaign simultaneously studied the atomic oxygen density and oxygen airglow intensity, and the analysis of these measurements resulted in consistent set of reaction rates describing O_2 nightglow excitation processes and quenching mechanisms (McDade et al., 1986b). Using the results from ETON, the atomic oxygen number density can be derived if the atmospheric number density and temperature are known (Murtagh, 1989;

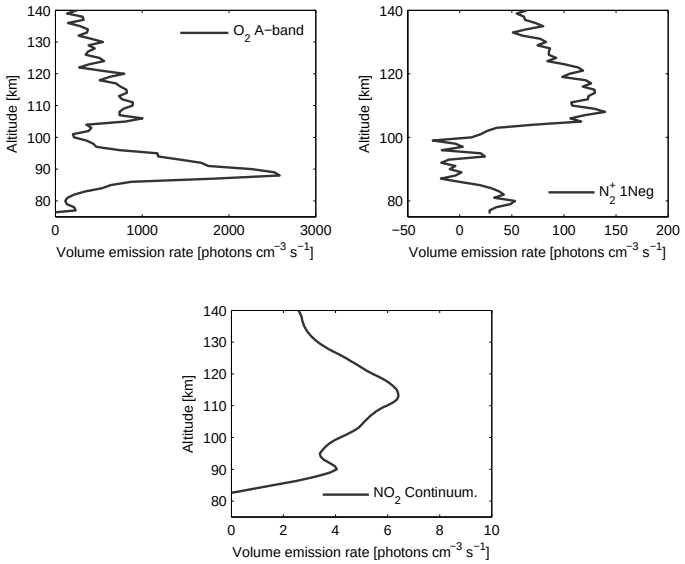

Figure 5: The retrieved volume emission rate profiles from the three NEMI photometers on the Hotel Payload 2 upleg. Right plot: O_2 atmospheric band emission at 762 nm, contaminated by aurora (N_2 1P band) above 100 km and with a clear peak at approximately 90 km. Middle plot: N_2^+ 1N emission at 391.4 nm. Left plot: The nightglow continuum emission at 540 nm, showing a peak at approximately 89 km and also probable auroral contamination above 100 km.

Hedin et al., 2009). Fig. 6, left plot, shows the retrieved oxygen number density profile, calculated using data from the ALOMAR sodium lidar as shown in Sect. 7 below. The error bars include uncertainties of both the rate coefficients and the Na lidar temperature. The peak number density is $3 \cdot 10^{11}$ cm^{-3} at 89 km. Above 100 km the error in the retrieved atomic oxygen profile is large due to the low signal-to-noise ratio. The 1N and A-band profiles also both show auroral emissions above 100 km. It can concluded that the A-band profile is contaminated by N_2(1P) emissions in the filter passband. Since the emissions are weak at altitudes above 100 km it would be difficult to calculate volume emission profiles also in the absence of auroral contamination. Therefore this contamination is not a major problem.

3.2. NO profile retrieval

Atomic oxygen is also responsible for the NO_2 nightglow continuum as this emission is produced in the NO + O air-afterglow reaction. With the atomic oxygen profile retrieved from the O_2 atmospheric band measurement the concentration of NO can be derived. The nightglow continuum has been studied from ground (e.g. Krassovsky and Shefov, 1965; Sternberg and Ingham, 1972; Gadsden and Marovich, 1973), from sounding rockets (e.g. Sharp, 1978; Witt et al., 1981; McDade et al., 1984; McDade et al., 1986a) and from satellites (e.g. von Savigny et al., 1999). The air- afterglow reaction is known to proceed along 2-body and 3-body paths simultaneously with one path dominating over the other depending on the third body number densities (Becker et al., 1970, 1972). At nightglow altitudes the third-body number densities are such that neither reaction path dominates over the other and both must be considered. Thus, if the air-afterglow reaction is solely responsible for the nightglow continuum, the local NO concentration is related to the NO_2 continuum volume emission rate, V_{cont}, and atomic oxygen concentration by $[\mathrm{NO}] = V_{\mathrm{cont}}/k[\mathrm{O}]$ where k is the combined 2-body and 3-body temperature dependent chemiluminescent rate coefficient (McDade et al., 1986a; von Savigny et al., 1999), shown in Fig. 6, middle plot. The derived nitric oxide density profile is shown in the right plot of Fig. 6. Above 100 km the signal is much stronger than expected, indicating auroral contamination also in this emission. This makes it impossible to derive the NO number density using the relation above. Thus, as seen from Fig. 6, middle plot, the 3-body air-afterglow reaction path is the significant one, with only a small contribution from the 2-body path. significant. The NO number density at

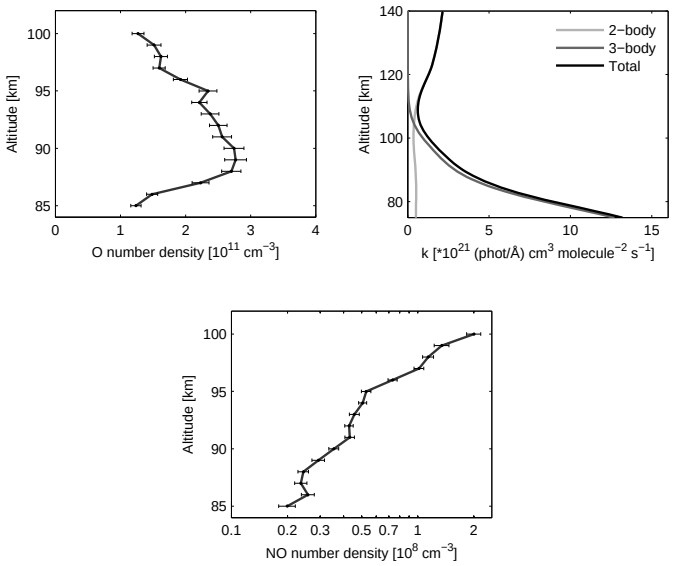

Figure 6: NEMI O and NO profile retrieval in the altitude range 85–100 km. Left plot: Retrieved [O] profile, error bars including uncertainties in rate coefficients and lidar temperature. Middle plot: 2-body, 3-body and combined chemiluminescent rate coefficient profile used in the retrieval of [NO] from the NO_2 continuum emission rate (Note the different altitude scale). Right plot: Retrieved [NO] profile. As is seen from the middle plot the 3-body reaction path is the most significant one below 100 km.

100 km is $1.8 \cdot 10^8$ cm^{-3}. In Fig. 9 the retrieved O and NO density profiles are also compared with model profiles, as described below in Sect. 6.

4. Faraday rotation and ion probe measurements

As mentioned the Hotel Payload 2 rocket carried Faraday rotation and positive ion probe measurements. The Faraday rotation measurement is based on the fact that a linearly polarised wave from a ground-based radio transmitter is a superposition of the circular `o` and `x` modes. In the ionosphere these have different refractive indices with respect to the electron gyro motion around the magnetic field lines which gives rise to a rotation of the plane of polarisation. This rotation can readily be measured by a dipole antenna on the spinning rocket (Mechtly et al., 1967). Electron densities calculated from Faraday rotation as well as positive ion number densities calculated from the

ion probe current are shown in Fig. 8 together with the coincident EISCAT measurements described in the following section. In the absence of negative ions the positive ion and electron densities must be identical. The discrepancy at 130–200 km is likely caused by payload charging affecting the positive ion probe. A possible discrepancy may also be seen below 90 km. Electron attachment to particles of meteoric origin may be part of the explanation for this. The presence of meteoric smoke particles in the mesopause region is a current topic of many studies, such as Rapp et al. (2010).

5. EISCAT measurements

During the launch day the Tromsø UHF radar was in its monthly 24-hour Common Programme experiment mode, providing a whole day of measurement time in addition to the campaign time. The radar experiment used was the *Beata* 32-bit alternating code programme, which is optimised for simultaneous E- and F-region auroral measurements (I. Häggström, private communication). The antenna scan pattern was the three-position CP2, alternating between magnetic zenith, vertical and low elevation eastward. Since Beata provides only short lags in the D region, an attempt at running a better D region experiment on the VHF radar was made during the launch, but this failed due to interference from the new collocated MORRO HF radar, which operates at 56 MHz (C. La Hoz, personal communication), i.e. exactly two octaves below the VHF at 224 MHz.

The Beata data were analysed with the standard EISCAT analysis software, GUISDAP (Fig. 7). The GUISDAP fitted electron densities from the time around the HotPay 2 launch are also shown in Fig. 8 as dots, the colours of the dots (visible in the online version of this paper) annotating the three different antenna positions. The theory used in GUISDAP usually works well in the E region and above, producing useful fits. Basically the short lags of the radar code give a pseudo raw power which is proportional to the electron density. In the D region however the fits failed, which is due to many factors: the poor signal to noise ratio in the absence of excess D-region ionisation (such as energetic aurora), the Beata code not providing long lags from the lower ranges, and to the GUISDAP IS theory being insufficient for the highly collisional D-region plasma, where also negative ions and meteoric smoke particles may be present. Therefore these points have been excluded. During the days after the flight, strong daytime electron precipitation appeared when the VHF radar was operating. This will allow retrieval of the

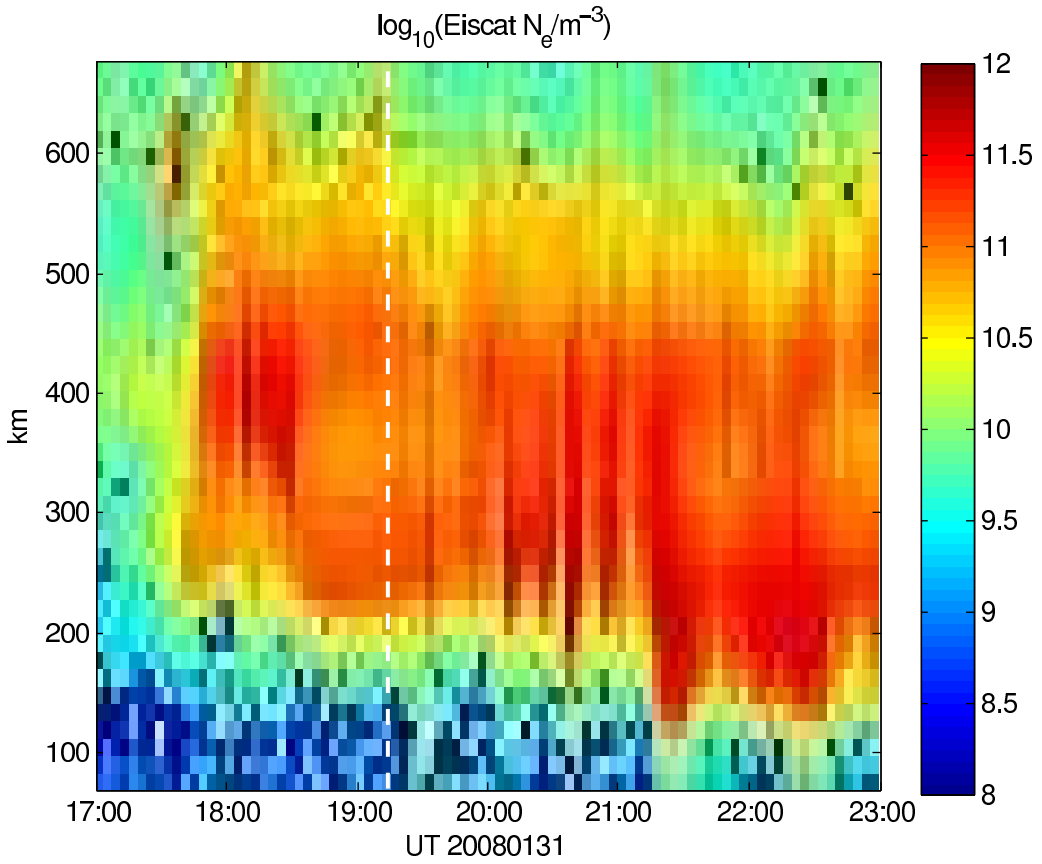

Figure 7: EISCAT GUISDAP electron density analysis of the Beata-CP2 common programme experiment for the evening of 20080131. Only data from the field-aligned position of the antenna scan are shown.

IS spectral shape in the D region, which may also be used as an indication of the possible presence of meteoric smoke particles (e.g. Fentzke et al., 2009).

6. SIC modelling

The Sodankylä coupled Ion-neutral time-dependent Chemistry (SIC) model is a tool developed for estimating the chemical effects of short-lived excess (i.e. additional to photochemical) ionisation and dissociation, caused by events such as particle precipitation (Verronen, 2006; Seppälä, 2007) and X-ray flares (Enell et al., 2008). SIC research mainly focuses on changes in

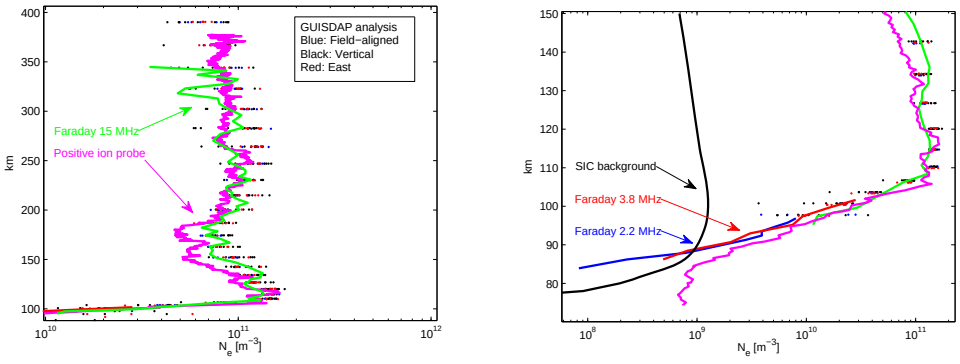

Figure 8: Summary of the Hotel Payload 2 electron and ion density measurements. Left plot: HotPay 2 Faraday electron density and positive ion density, as well as EISCAT GUISDAP electron density for times close to the launch, in the altitude range 100–400 km. The GUISDAP electron density measurements are colour-coded (see online version) according to antenna scan position: Blue=field-aligned, black=vertical, red=eastward; Right panel: Scale restricted to the height interval 70–150 km.

odd nitrogen and odd hydrogen and consequent ozone loss in the mesosphere, where results have been verified carefully especially in the case of solar proton events, for example with Envisat/GOMOS (Verronen, 2006; Seppälä et al., 2008).

SIC is a conceptually simple but comprehensive, fully time-dependent 1-dimensional model of coupled ion and neutral chemistry, solving the differential equations for almost 400 reactions of 36 positive ions, 27 negative ions and 14 minor neutral components in the altitude range 20–150 km. The neutral background atmosphere is taken from MSISE-90 and Shimazaki (1984). The photochemistry in SIC is based on solar spectra which are usually taken from the Solar Irradiance Platform (SIP), a development of the Solar 2000 empirical model (see Tobiska et al., 2000). Radiative transfer and particle ionisation are calculated using relations found in Rees (1989). See the thesis by Verronen (2006) for more details on the model. From the SIC results the electron density is calculated as the difference between the total positive and negative ion concentrations.

Each SIC model run is initiated by a control run, starting from arbitrary concentration profiles of all modelled species and repeating one diurnal cycle, with photochemistry only, until a quasi-steady state is reached. This

procedure converges slowly for midwinter runs but as long as changes in the quantities we study here, electron density and [NO], the control run is considered successful. In this study it was natural to use the geographical coordinates of the EISCAT radar site (69.48° N, 19.22° E). The MSISE-90 model takes the 10.7 cm solar flux and a_{p} index as inputs, but their effect on the profiles below 100 km is small.

For the scenario runs the rate of additional electron ionisation, q, is divided into individual ionisation rates of the main constituents N_2, O_2 and O. Dissociation of N_2, and its branching ratio into the $N(^2D)$ state which is a source of NO, is also parametrised from q (Rusch et al., 1981). We here applied an iterative search for q in the SIC model, searching for the rate that reproduced $\frac{dN_{\mathrm{e}}}{dt}$ as estimated from smoothed EISCAT profiles. It must be noted that this procedure relies on the Eulerian assumption $\frac{DN_{\mathrm{e}}}{Dt} = \frac{dN_{\mathrm{e}}}{dt}$, i.e. that the same air mass is observed during the whole experiment, as discussed at some length by Semeter and Kamalabadi (2005). As seen from the meteor radar measurements described in the following section the rocket flight took place during the zero crossing of the 12-hour tide, so the horizontal wind was weak.

Fig. 9 shows the nitric oxide variation calculated by this SIC model run. Large increases due to aurora are seen mainly after 21 UT. The SIC background and NEMI results should therefore be comparable. The N_{e} background profile from 19:15 UT in the 18th cycle of the SIC control run is also shown in Fig. 8, together with the Faraday profiles and EISCAT results. The [NO], [O] and N_{e} profiles all differ significantly except for the O concentration at the peaks of the profiles. From the ground based wind measurements and coincident satellite measurements it is clear that these discrepancies are caused by the large-scale dynamics of the winter polar vortex.

7. Atmospheric conditions and dynamics

The zonal and meridional winds were measured by the continuously running SKiYMET meteor radar at Andenes (Singer et al., 2003, 2004), Fig. 10. From the horizontal wind a first-order back trajectory estimate (not shown) indicates that the air mass of the flight came from above northern Scandinavia. As can be seen the 12-hour tide dominated the horizontal wind in the UMLT region, as expected. During the time of the launch the tide was at the turning phase, horizontal winds close to zero. Therefore the EISCAT and

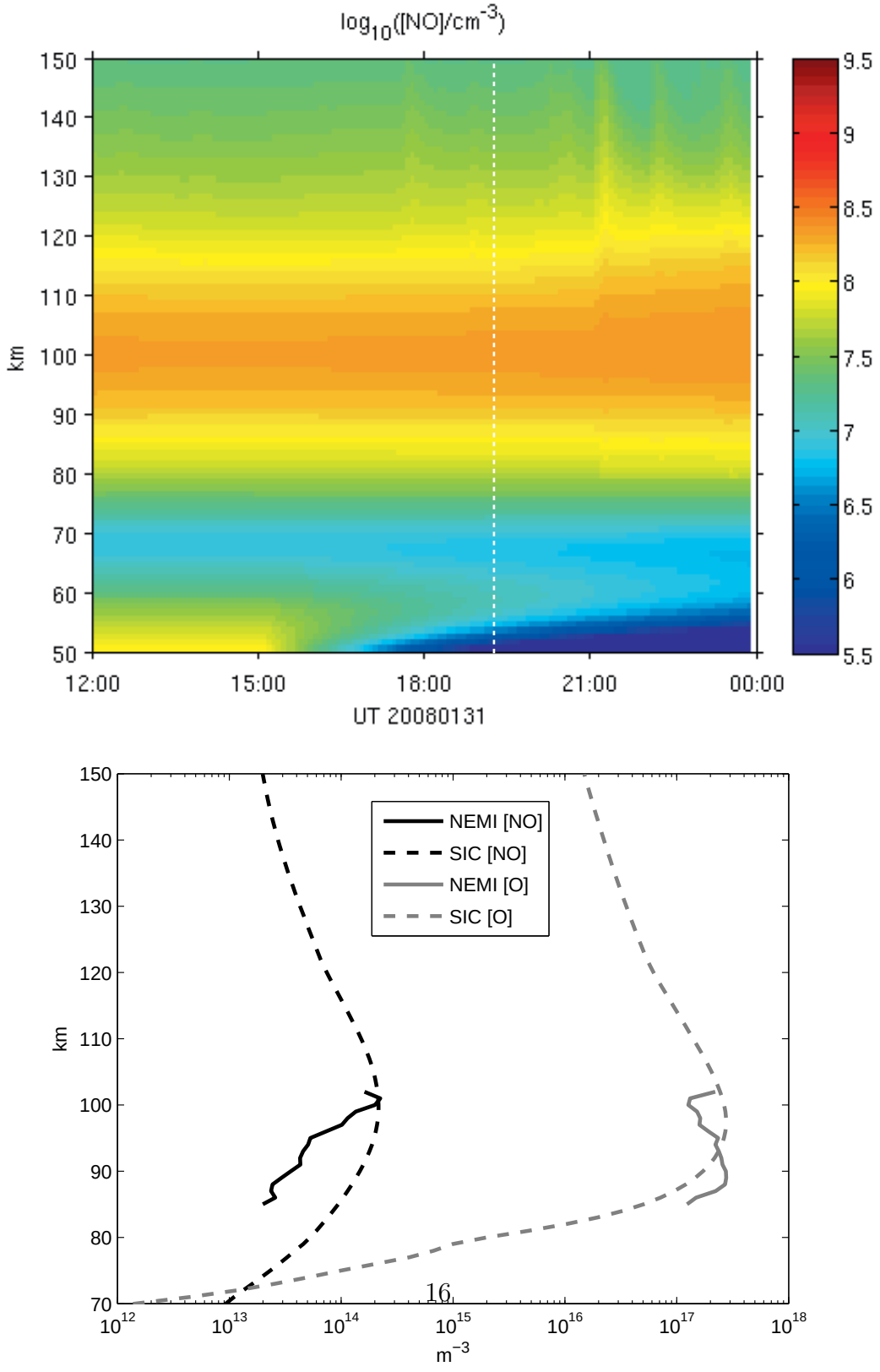

Figure 9: SIC model runs with iterative search for ionisation rate, based on $\frac{dN_e}{dt}$ estimated from EISCAT (GUISDAP analysed Ne). The EISCAT Ne profiles have been smoothed by a 3rd degree polynomial fit in altitude and median filtering in time before the numerical differentiation. Upper plot: Electron density profiles. Lower plot: Comparison between modelled and measured [NO] and [O] profiles from NEMI, 19:15 UT.

HotPay 2 measurements should be comparable in the absence of structured auroral precipitation and other small-scale perturbations.

Fig. 11, left panel, shows temperature profiles measured with the ALOMAR Na lidar during the day of the HotPay 2 launch. In the right panel the 10-minute average profile around the time of launch is shown together with the the MSISE-90 model temperature profile used for the SIC modelling in the SIC range 20–150 km. It is likely that MSISE-90 is not representative of the deep solar minimum thermosphere of 2008, as the average temperature as indicated by the lidar is some 10 K lower. An apparent perturbation with a vertical wavelength of about 5.5 km and an amplitude of 7–8 K is also seen. The smaller wave-like variations of 1–2 K amplitude and about 1 km vertical wavelength are near the instrument's resolution limit and likely due to photon shot noise.

Temperature perturbations similar to the difference between the lidar and MSIS temperature were imposed on the SIC model to study whether the temperature dependence of the reaction rates alone could cause discrepancies of this magnitude, but this cannot be the case. This gives further confirmation that dynamic processes, that is, meridional transport and subsidence in the polar vortex, control the nitric oxide and oxygen profiles. Satellite measurements also indicate thermosphere-mesosphere exchange in vortex filaments, as show in next section.

8. SciSat ACE NO measurements

Remote sensing of nitric oxide from satellites is possible both in the thermosphere above the lower-thermospheric NO maximum using the γ band emission in the UV dayglow, the SNOE satellite being a well-known example (e.g. Solomon et al., 1999), and in the middle atmosphere by means of infrared absorption spectroscopy. The Atmospheric Chemistry Experiment Fourier Transform Spectrometer (ACE-FTS) on board the Canadian SciSat (Bernath et al., 2005) is one of few currently operating instruments capable of measuring nitric oxide profiles by solar occultation spectroscopy. The instrument is a Fourier transform spectrometer operating in the IR range 2.2–13.3 μm. Fig. 12 shows the [NO] profiles from a latitude of close to 66°, i.e. close to the latitude of Andøya and EISCAT. The profile from closest in longitude is shown separately in the right panel. Kerzenmacher et al. (2008) discuss validation of the FTS NO profiles. At the profile minimum, 60–80 km, the errors are large, as evident also from this profile. At the peak

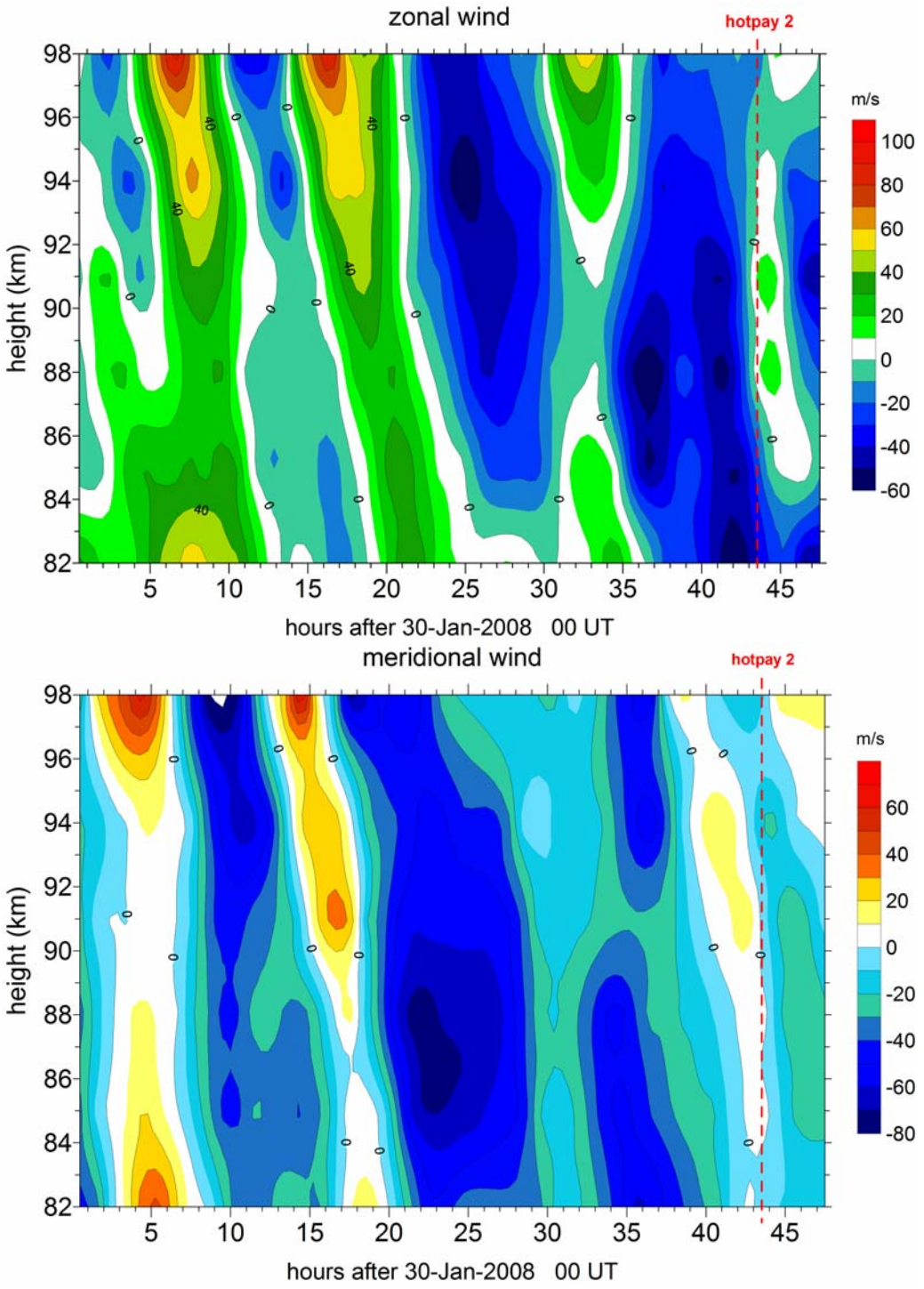

Figure 10: Andøya meteor radar wind measurements. Upper panel: Zonal winds. Lower panel: Meridional winds. The line marks the time of the rocket launch.

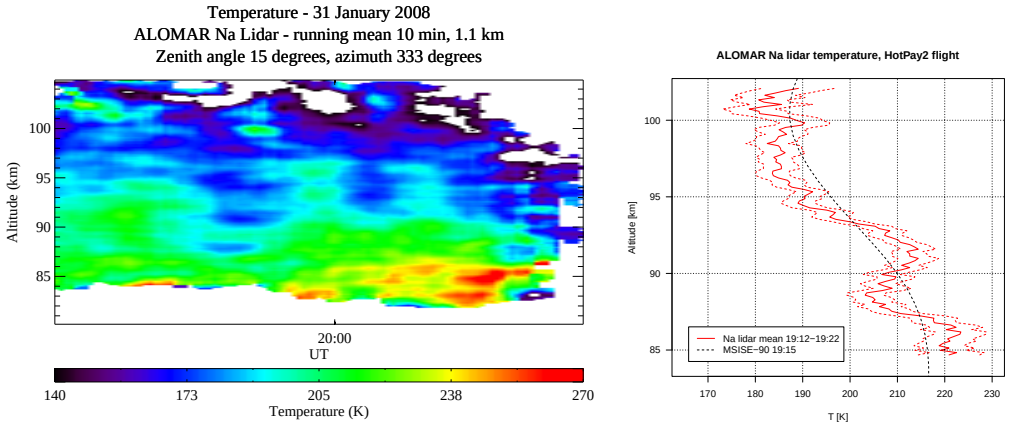

Figure 11: ALOMAR Na lidar temperature analyses. Left panel: 10-minute average analyses for the Hotel Payload 2 launch day. Right: The 10-minute average profile 19:12–19:22 UT shown together with the MSISE-90 temperature profile used in the SIC modelling.

the errors are smaller but the ACE profiles still deviate from those of other instruments such as HALOE. However, a longitudinal variation is seen and at some longitudes also evidence of subsidence. The results compare well with EOS Aura microwave limb sounder (MLS) quick-look data (available at `http://mls.jpl.nasa.gov/`) from the 2700 K potential temperature level (near 60 km), where vortex patches northwest of N Norway show elevated temperatures and carbon monoxide (CO) mixing ratios as well as low water vapour mixing ratios, confirming the subsidence of thermospheric air.

9. Discussion and conclusions

The profiles measured by HotPay 2/NEMI are downshifted as compared with the profiles measured by earlier rocket instruments such as ETON (McDade et al., 1986a). The SIC model quasi-steady-state background NO number density profile is also clearly overestimated. This suggests that subsidence over the winter pole is not compensated by meridional transport during the cold and geomagnetically quiet period preceding the campaign. The flight took place after the passage of a quiet auroral arc. Although the aurora controlled the E and F layer electron densities after 17:30 UT, as seen from the EISCAT measurements (Fig. 7), the precipitation was not sufficiently energetic to affect the UMLT region. Local effects of energetic precipitation preceding the measurements can therefore be excluded and the composition

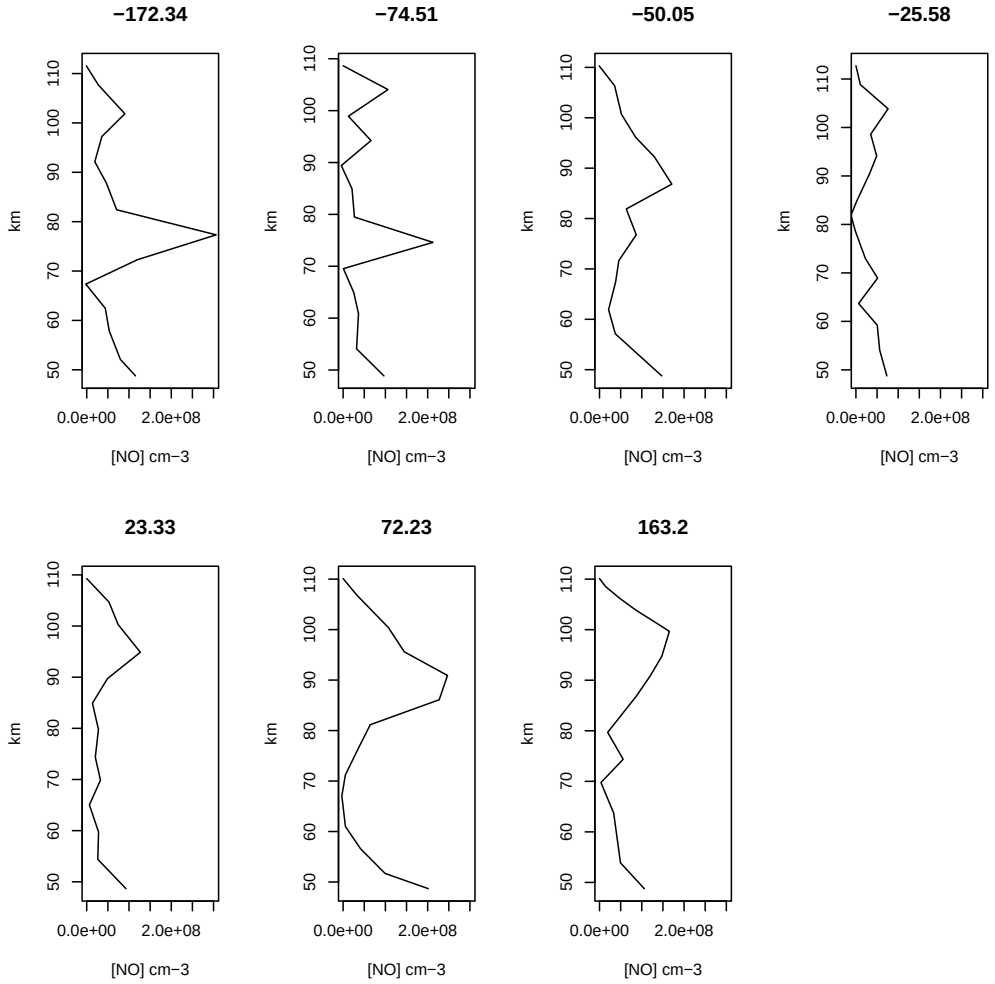

Figure 12: SciSat ACE-FTS nitric oxide profiles at a latitude of 66 degrees and 7 different longitudes. The longitudinal transect clearly shows the variation in NO in the UMLT caused by meridional transport and subsidence.

was dominated by large-scale dynamics. The ACE [NO] profile from the longitude closest to the HotPay 2 flight agrees with the NEMI profile in that the number density at 100 km is on the order of 10^8 cm^{-3}. At some longitudes the ACE NO peak was also shifted down to altitudes in the range 70–90 km. The ACE-FTS data therefore further confirm that the UMLT nitric oxide profile observed at the time of the HotPay 2 was not much affected by the weak aurora which appeared before the flight after the long quiet period, but controlled by transport from lower latitudes and subsidence over the pole. The NEMI experiment, as well as satellite data, therefore give clear evidence of the importance of downward transport from the lower thermosphere into the middle atmosphere in the winter polar vortex. Any local measurements and modelling should take large-scale dynamics into account as necessary.

On the other hand, energetic electron precipitation directly affecting the UMLT altitude region did appear later during the continued Hotel Payload 2 ground-based measurement campaign in early February 2008. Refined analysis of daytime EISCAT VHF data from this period will allow estimating, among other phenomena, the presence of meteoric smoke particles, which may explain parts of the discrepancy between the measured positive ion and electron density profiles. This topic is beyond the scope of this paper but subject to further investigation by the present authors and collaborators (e.g. Friedrich et al., 2010; Strelnikova and Rapp, 2010). Especially interesting is that 3-D imaging optical and radar instruments are or will be available for the purpose of UMLT studies. We aim at developing the use of such data for remote sensing of NO and other aspects of UMLT composition such as the presence of negative ions and meteoric particles in the D region.

Acknowledgements

The Hotel Payload rocket launch from Andøya Rocket Range was funded by the European Union FP6 programme through the project RITA-CT-2003-506208 (ALOMAR eARI - enhanced Access to Research Infrastructure). The authors thank the staff at ARR and ALOMAR for assistance in the project. U.-P. Hoppe and B. Kaifler thank C.-Y. She and CSU colleagues, B.P. Williams, NWRA/CoRA Division for the fruitful collaboration concerning the Na Lidar at ALOMAR. UPH and BK are grateful to G. von Cossart and IAP Kühlungsborn for generous collaboration on the ALOMAR lidar telescopes and the spectrum analyzer.

In the progress of this work Carl-Fredrik Enell and Antti Kero have been supported by the Academy of Finland through the research projects 1109054 - Solar Energetic Radiation and Chemical Aeronomy of the Mesosphere, and 11232755 - Thermosphere and Mesosphere affecting the Stratosphere. AK is currently funded by project 134439, Negative Ion Chemistry Effects in Mesospheric Active Heating Experiments. CFE also gratefully acknowledges travel support from the Network for Groundbased Optical Auroral Research in the Arctic Region (NordAuropt) financed by the Nordic Council of Ministers.

The European Incoherent Scatter Scientific Association (EISCAT) is an international research organisation operating three incoherent scatter radar systems and an ionospheric heater in Northern Scandinavia. It is funded and operated by the research councils of Norway, Sweden, Finland, Japan, China, the United Kingdom and Germany.

References

Becker, K.H., Groth, W., Thran, D., 1970. The airglow reaction NO + O + (M) $\rightarrow$ NO_2^* + (M) at low pressure. Chem. Phys. Lett. 6, 583.

Becker, K.H., Groth, W., Thran, D., 1972. The mechanism of the air-afterglow NO + O $\rightarrow$ NO_2 + $h\nu$. Chem. Phys. Lett. 15, 215.

Bernath, P.F., McElroy, C.T., Abrams, M.C., Boone, C.D., Butler, M., Camy-Peyret, C., Carleer, M., Clerbaux, C., Coheur, P.F., Colin, R., DeCola, P., DeMazière, M., Drummond, J.R., Dufour, D., Evans, W.F.J., Fast, H., Fussen, D., Gilbert, K., Jennings, D.E., Llewellyn, E.J., Lowe, R.P., Mahieu, E., McConnell, J.C., McHugh, M., McLeod, S.D., Michaud, R., Midwinter, C., Nassar, R., Nichitiu, F., Nowlan, C., Rinsland, C.P., Rochon, Y.J., Rowlands, N., Semeniuk, K., Simon, P., Skelton, R., Sloan, J.J., Soucy, M.A., Strong, K., Tremblay, P., Turnbull, D., Walker, K.A., Walkty, I., Wardle, D.A., Wehrle, V., Zander, R., Zou, J., 2005. Atmospheric Chemistry Experiment (ACE): Mission overview. Geophys. Res. Lett. 32, L15S01.

Brändström, U., 2003. The Auroral Large Imaging System — Design, operation and scientific results. Ph.D. thesis. Swedish Institute of Space Physics. Kiruna, Sweden. IRF Scientific Report 279, ISBN: 91-7305-405-4.

Enell, C.F., Verronen, P.T., Beharrell, M.J., Vierinen, J.P., Kero, A., Seppälä, A., Honary, F., Ulich, T., Turunen, E., 2008. Case study of the mesospheric and lower thermospheric effects of solar X-ray flares: Coupled ion-neutral modelling and comparison with EISCAT and riometer measurements. Ann. Geophys. 26, 2311–2321.

Fentzke, J.T., Janches, D., Strelnikova, I., Rapp, M., 2009. Meteoric smoke particle properties derived using dual-beam Arecibo UHF observations of D-region spectra during different seasons. J. Atmos. Sol.-Terr. Phys. 71, 1982–1991.

Friedrich, M., Rapp, M., Plane, J.M.C., Torkar, K.M., 2010. Bite-outs and other depletions of mesospheric electrons. J. Atmos. Sol.-Terr. Phys. Accepted.

Gadsden, M., Marovich, E., 1973. The nightglow continuum. J. Atmos. Terr. Phys. 35, 1601.

Greer, R.G.H., Murtagh, D.P., McDade, I.C., Dickinson, P.H.G., Thomas, L., Jenkins, D.B., Stegman, J., Llewellyn, E.J., Witt, G., Mackinnon, D.J., Williams, E.R., 1986. ETON 1: a database pertinent to the study of energy transfer in the oxygen nightglow. Planet. Space Sci. 34, 771.

Hedin, J., Gumbel, J., Stegman, J., Witt, G., 2009. Use of O_2 airglow for calibrating direct atomic oxygen measurements from sounding rockets. Atm. Meas. Tech. 2, 801–812.

Jacobsen, T.A., Friedrich, M., 1979. Electron density measurements in the lower D-region. J. Atmos. Terr. Phys. 41, 1195–1200.

Kerzenmacher, T., Wolff, M.A., Strong, K., Dupuy, E., Walker, K.A., Amekudzi, L.K., Batchelor, R.L., Bernath, P.F., Berthet, G., Blumenstock, T., Boone, C.D., Bramstedt, K., Brogniez, C., Brohede, S., Burrows, J.P., Catoire, V., Dodion, J., Drummond, J.R., Dufour, D.G., Funke, B., Fussen, D., Goutail, F., Griffith, D.W.T., Haley, C.S., Hendrick, F., Höpfner, M., Huret, N., Jones, N., Kar, J., Kramer, I., Llewellyn, E.J., López-Puertas, M., Manney, G., McElroy, C.T., McLinden, C.A., Melo, S., Mikuteit, S., Murtagh, D., Nichitiu, F., Notholt, J., Nowlan, C., Piccolo, C., Pommereau, J.P., Randall, C., Raspollini, P., Ridolfi, M., Richter, A., Schneider, M., Schrems, O., Silicani, M., Stiller, G.P., Taylor, J., Tétard,

C., Toohey, M., Vanhellemont, F., Warneke, T., Zawodny, J.M., Zou, J., 2008. Validation of NO_2 and NO from the Atmospheric Chemistry Experiment (ACE). Atmos. Chem. Phys. 8, 5801–5841.

Krassovsky, V.I., Shefov, N.N., 1965. Airglow. Space Science Rev. 4, 176.

Lynch, K.A., Gelinas, L.J., Kelley, M.C., Collins, R.L., Widholm, M., Rau, D., MacDonald, E., Liu, Y., Ulwick, J., Mace, P., 2005. Multiple sounding rocket observations of charged dust in the polar winter mesosphere. J. Geophys. Res. 110.

McDade, I.C., Greer, G.H., Murtagh, D.P., 1984. Thermospheric nitric oxide concentrations derived from a measurement of the altitude profile of the green nightglow continuum. Ann. Geophys. 2, 487–493.

McDade, I.C., Llewellyn, E.J., Greer, R.G.H., Murtagh, D.P., 1986a. ETON 3: Altitude profiles of the nightglow continuum at green and near infrared wavelengths. Planet. Space Sci. 34, 801–810.

McDade, I.C., Murtagh, D.P., Greer, R.G.H., Dickinson, P.H.G., Witt, G., Stegman, J., Llewellyn, E.J., Thomas, L., Jenkins, D.B., 1986b. ETON 2: Quenching parameters for the proposed precursors of $O_2(b^1\Sigma_g^+)$ and $O(^1S)$ in the terrestrial nightglow. Planet. Space Sci. 34, 789–800.

McLean, S., Macmillan, S., Maus, S., Lesur, V., Thomson, A., Dater, D., 2004. The US/UK World Magnetic Model for 2005–2010. NOAA Technical Report NESDIS/NGDC. NOAA NGDC.

Mechtly, E.A., Bowhill, S.A., Smith, L.G., Knoebel, H.W., 1967. Lower ionosphere electron concentrations and collision frequency from rocket measurements of Faraday rotation, differential absorption, and probe current. J. Geophys. Res. 72, 5239–5245.

Meriwether Jr., J.W., 1989. A review of the photochemistry of selected nightglow emissions from the mesopause. J. Geophys. Res. 94, 14639–14646.

Murtagh, D.P., 1989. A self-consistent model of the most common nightglow emissions, in: Burke, W.R. (Ed.), Proc. 9th ESA PAC symposium, European Space Agency. pp. 167–171.

474 Rapp, M., Strelnikova, I., Strelnikov, B., Hoffmann, P., Friedrich, M., Gum-
475 bel, J., Megner, L., Hoppe, U.P., Robertson, S., Knappmiller, S., Wolff, M.,
476 Marsh, D.R., 2010. Rocket-borne in situ measurements of meteor smoke:
477 Charging properties and implications for seasonal variation. J. Geophys.
478 Res. 115, D00I16.

479 Rees, M.H., 1989. Physics and Chemistry of the Upper Atmosphere. Cam-
480 bridge University Press, Cambridge, UK.

481 van Rhijn, P.J., 1921. On the brightness of the sky at night and the total
482 amount of starlight. volume 31 of *Publ. Astr. Lab. Groningen.* Hoitsema
483 Brothers, Groningen.

484 Rietveld, M.T., Kohl, H., Kopka, H., Stubbe, P., 1992. Introduction to
485 ionospheric heating at Tromsø-I. Experimental overview. J. Atmos. Terr.
486 Phys. 55, 577–599.

487 Rusch, D.W., Gérard, J.C., Solomon, S., Crutzen, P.J., Reid, G.C., 1981.
488 The effect of particle precipitation events on the neutral and ion chemistry
489 of the middle atmosphere–I. Odd nitrogen. Planet. Space Sci. 29, 767 –
490 774.

491 von Savigny, C.H.A., McDade, I.C., Shepherd, G.G., Rochon, Y., 1999.
492 Lower thermospheric nitric oxide concentrations derived from WINDII ob-
493 servations of the green nightglow continuum at 553.1 nm. Ann. Geophys.
494 17, 1439–1446.

495 Semeter, J., Kamalabadi, F., 2005. Determination of primary electron spec-
496 tra from incoherent scatter radar measurements of the auroral E region.
497 Radio Sci. 40, RS2006.

498 Seppälä, A., 2007. Observations of production and transport of NOx formed
499 by energetic particle precipitation in the polar night atmosphere. Ph.D.
500 thesis. Finnish Meteorological Institute. Yliopistopaino, Helsinki, Finland.
501 ISBN: 978-952-10-4181-5 (PDF).

502 Seppälä, A., Randall, C.E., Clilverd, M.A., Rozanov, E., Rodger, C.J., 2009.
503 Geomagnetic activity and polar surface air temperature variability. J.
504 Geophys. Res. 114.

505 Seppälä, A., Rodger, C.J., Clilverd, M.A., Verronen, P.T., Turunen, E., 2008.
506 The effects of hard spectra solar proton events on the middle atmosphere.
507 J. Geophys. Res. 113, A11311.

508 Seppälä, A., Verronen, P.T., Clilverd, M.A., Randall, C.E., Tamminen, J.,
509 Sofieva, V., Backman, L., Kyrölä, E., 2007. Arctic and Antarctic polar
510 winter NO_x and energetic particle precipitation in 2002–2006. Geophys.
511 Res. Lett. 34, 12810.

512 Sharp, W.E., 1978. NO_2 continuum in aurora. J. Geophys. Res. 83, 4373.

513 Shimazaki, T., 1984. Minor Constituents in the Middle Atmosphere. Num-
514 ber 6 in Developments in Earth and Planetary Physics, D. Reidel Publish-
515 ing Company.

516 Singer, W., Bremer, J., Hocking, W.K., Weiss, J., Latteck, R., Zecha, M.,
517 2003. Temperature and wind tides around the summer mesopause at mid-
518 dle and arctic latitudes. Adv. Space Res. 31, 2055–2060.

519 Singer, W., Weiß, J., von Zahn, U., 2004. Diurnal and annual variations of
520 meteor rates at the arctic circle. Atmos. Chem. Phys. 4, 1355–1363.

521 Solomon, S.C., Barth, C.A., Bailey, S.M., 1999. Auroral production of nitric
522 oxide measured by the SNOE satellite. Geophys. Res. Lett. 26, 1259–1262.

523 Sternberg, J.R., Ingham, M.F., 1972. Observations of the airglow continuum.
524 Mon. Not. R. astr. Soc. 159.

525 Strelnikova, I., Rapp, M., 2010. Studies of polar mesosphere summer echoes
526 with the EISCAT VHF and UHF radars: Information contained in the
527 spectral shape. Adv. Space Res. 45, 247–259.

528 Tobiska, W., Woods, T., Eparvier, F., Viereck, R., Floyd, L., Bouwer, D.,
529 Rottman, G., White, O., 2000. The SOLAR2000 empirical solar irradiance
530 model and forecast tool. J. Atmos. Sol.-Terr. Phys. 62, 1233–1250.

531 Vallance-Jones, A., 1974. Aurora. volume 9 of *Geophysics and astrophysics*
532 *monographs*. D. Reidel Publishing Company. ISBN: 90-277-0272-1.

533 Verronen, P.T., 2006. Ionosphere-atmosphere interaction during solar proton
534 events. Ph.D. thesis. Finnish Meteorological Institute. Helsinki, Finland.
535 ISBN: 951-697-650-6.

536 Witt, G., Rose, J., Llewellyn, E.J., 1981. The airglow continuum at high
537 latitudes — an estimate of the NO concentration. J. Geophys. Res. 86,
538 623–628.